Supplementary Materials

Proton tunneling interfacial engineering enables selective CO_2 electroreduction on CoZn oxide nanoflowers

Yingxia Hu[#], Nan Wang[#], Xidong Lin*, Qingxia Liu*

Future Technology School, Shenzhen Technology University, Shenzhen 518118, Guangdong, China.
[#]Authors contributed equally.

***Correspondence to:** prof. Qingxia Liu, Dr. Xidong Lin, Future Technology School, Shenzhen Technology University, Shenzhen 518118, Guangdong, China. E-mail: liuqingxia@sztu.edu.cn; linxidong@sztu.edu.cn

EXPERIMENTAL SECTION

Statistical analysis was performed using OriginPro 2021. All data are presented as mean ± standard deviation (SD) from n = 3 independent replicates. Statistical significance between groups was determined using a two-tailed unpaired Student's t-test. A P value of less than 0.05 was considered statistically significant ($P < 0.05$, $P < 0.01$, $P < 0.005$) For in situ ATR-FTIR studies, A custom three-electrode spectro-electrochemical cell with a working volume of approximately 2-3 mL was employed. The working electrode was fabricated by applying a catalyst film onto a gold-sputtered silicon prism. The electrochemical environments consisted of two separate electrolyte systems: (i) 0.1 M $KHCO_3$ aqueous solution saturated with CO_2, and (ii) the hybrid electrolyte system composed of 0.06 M $KHCO_3$ +0.1 M [EMIM]Cl saturated with CO_2. The spectra shown in Figure 5 compare the intermediate stabilization in the two electrolyte environments. First-principles density functional theory (DFT) calculations were performed using the Vienna Ab initio Simulation Package (VASP) [1] with the projector augmented wave (PAW) method [2]. The exchange-functional was treated within the generalized gradient approximation (GGA) employing the Perdew-Burke-Ernzerhof (PBE) functional[3]. The long-range van der Waals interaction is described by the DFT-D3

approach[4]. A plane wave basis set with an energy cutoff of 400 eV was employed, and the geometry relaxation was performed until the forces on each atom were below 0.03 eV/Å. Self-consistent calculations were conducted with an energy convergence threshold of 10^{-5} eV.

The Gibbs free energy was calculated using the following equation (Eq. S1):

$$G = E_{DFT} + H(T) - TS = E_{DFT} + ZPE + \Delta U(0\text{-}T) - TS \qquad \text{Eq. S1[5]}$$

where E_{DFT} represents the total energy obtained from DFT calculations for each species, ZPE is the zero-point energy, $\Delta U(0\text{-}T)$ denotes the internal energy change from 0 K to the target temperature T (298.15 K), and S is the entropy at 298.15 K.

The values of ZPE, $\Delta U(0\text{-}T)$, and TS were derived from vibrational frequency calculations performed within the DFT framework. These thermodynamic corrections were evaluated for each adsorbed intermediate and gas-phase reference using VASPKIT version 1.5.1[5].

The AIMD simulations were carried out by the CP2K 2025.1 package[6]. The Perde-Burke-Ernzerhof (PBE) [7] function density functional corrected by the empirical dispersion corrections of Grimme's D3[8] was employed. To accurately depict the potential near nuclei, Goedecker-Teter-Hutter (GTH) pseudopotentials were employed. A mixed Gaussian and plane wave (GPW) approach was taken, where double-ζ valence augmented with polarization (DZVP) Gaussian basis sets were adopted, and the plane wave (PW) expansion of the charge density with a cutoff energy of 500 Ry. Besides, the AIMD simulations were performed in a canonical ensemble (NVT) at 298.15 K with a CSVR thermostat to regulate the temperature. The time step for the motion of nuclei in AIMD is 0.5 fs.

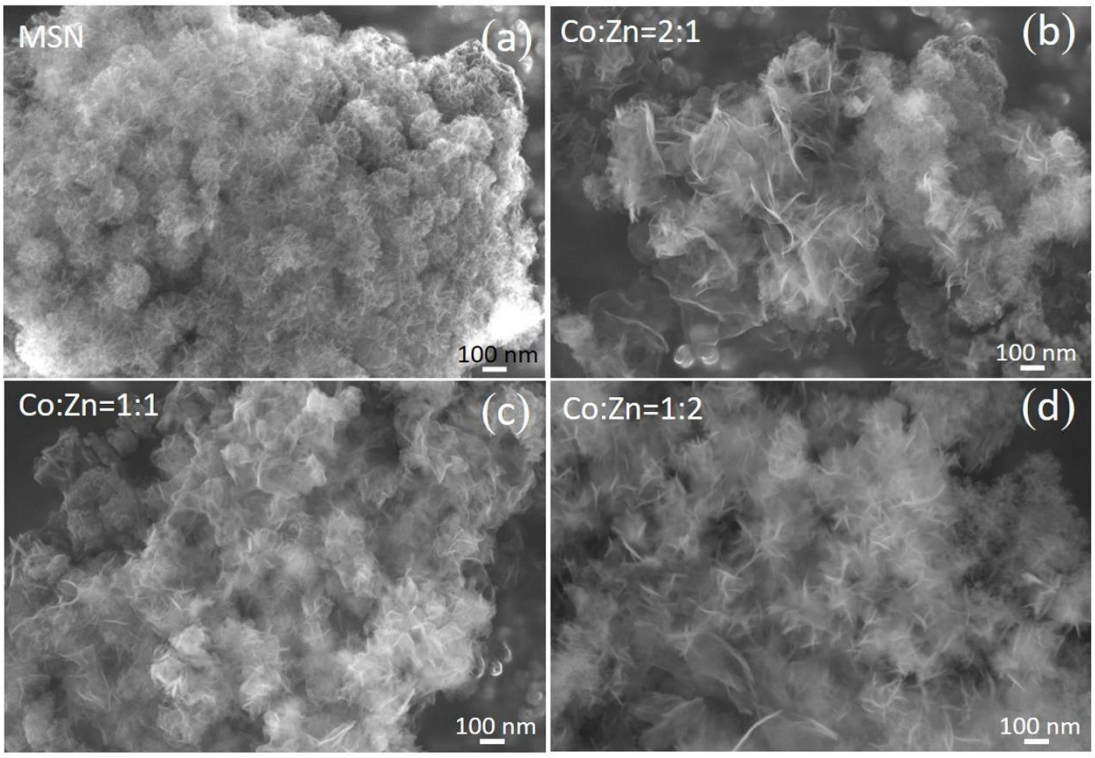

Figure s1. (a) Scanning electron microscopy (SEM) image of the freestanding porous silicon nanospheres as template. (b-d) SEM images of the three-dimensional flower-like hierarchical catalysts synthesized via template-assisted method with tunable Co/Zn molar ratios.

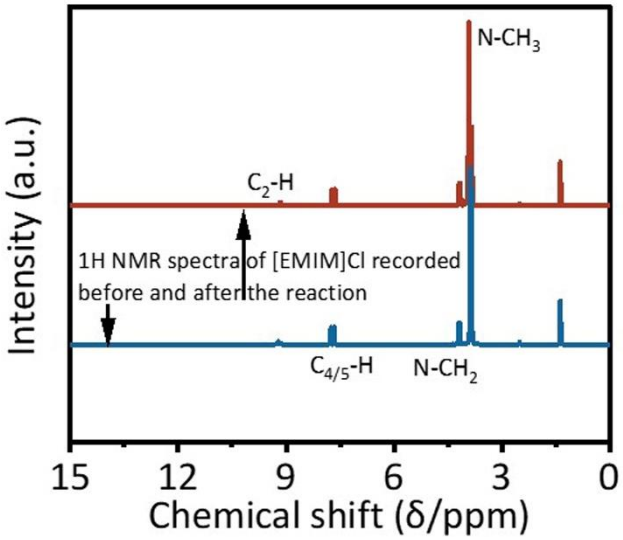

Figure s2. ^{1}H NMR spectra of the [EMIM]Cl/$KHCO_3$ hybrid electrolyte before (red trace) and after (blue trace) 12 h continuous CO_2 electroreduction chronoamperometry at -0.8 V vs. RHE over Co:Zn = 2:1 catalyst.

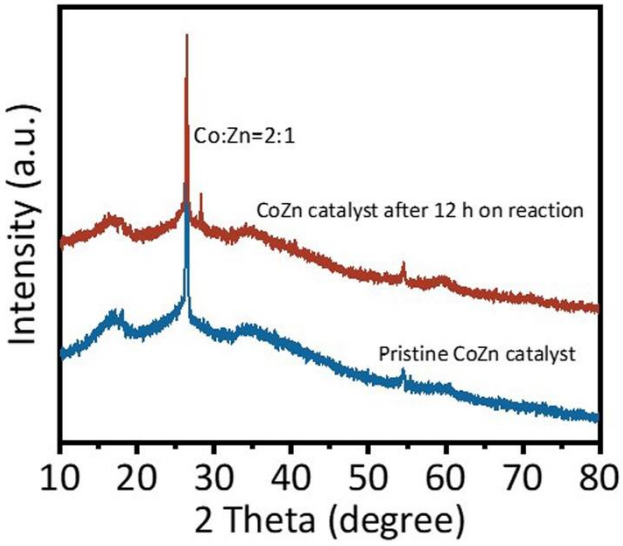

Figure s3. XRD patterns of the pristine Co:Zn=2:1 bimetallic oxide catalyst (blue curve) and spent catalyst recovered after 12 h continuous CO_2 electroreduction at -0.8 V vs. RHE (red curve).

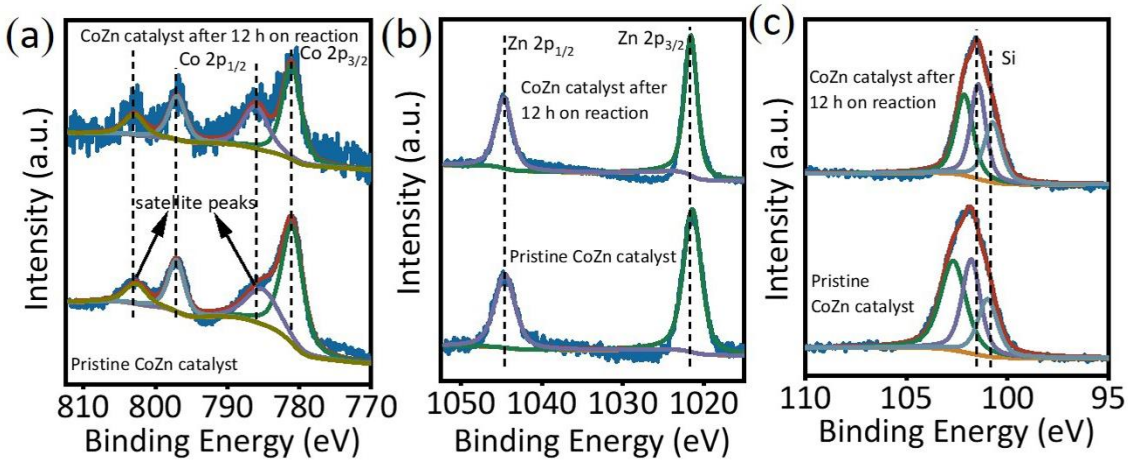

Figure s4a-c. High-resolution XPS spectra of (a) Co 2p, (b) Zn 2p, and (c) Si reference peak for pristine Co:Zn=2:1 oxide catalyst and spent catalyst after 12 h CO_2RR electrolysis at -0.8 V vs. RHE. (a) The Co 2p spectrum of post-reaction catalyst displays weak low-binding-energy shoulders alongside the characteristic satellite peaks of Co oxide, confirming partial surface reduction of Co cations under cathodic polarization; (b) The Zn $2p_{3/2}$ and Zn $2p_{1/2}$ doublets show negligible shift and intensity variation before and after electrolysis; (c) The Si reference peak verifies consistent charge correction for all XPS datasets. Overall XPS results evidence only mild surface reconstruction without bulk phase transformation of the CoZn spinel oxide.

Table S1. Actual Co:Zn molar ratios of the three CoZn oxide nanoflower catalysts determined by ICP-OES analysis.

Catalyst ID	Nominal Co:Zn ratio	Actual Co:Zn ratio (ICP-OES)	Co content (wt%)	Zn content (wt%)
1	≈1:1	0.98: 1.00	8.42	8.59
2	≈2:1	1.95: 1.00	12.36	6.34
3	≈1:2	0.49: 1.00	5.18	10.57

Table S2. BET surface areas and total pore volumes of the three CoZn oxide nanoflower catalysts.

Catalyst ID	Nominal Co:Zn ratio	BET surface area (m^2/g)	Total pore volume (cm^3/g)	Mesopore size range/feature
1	≈1:1	165	0.45	Broad distribution, no pronounced peak
2	≈ 2:1	142	0.38	Narrow mesopores (10-20 nm)
3	≈ 1:2	186	0.57	Large mesopores (centered at ~50-60 nm)

The presence of nitrogen (N) in the elemental maps (Figure 1d) warrants clarification regarding its origin and potential influence on catalytic performance. The N signal

arises from two sources: residual cetyltrimethylammonium bromide (CTAB) template used in the MSN support synthesis, and urea employed as a precipitating agent during the CoZn oxide deposition. To quantify the N content and assess its potential impact, we performed systematic XPS survey scans to determine the surface elemental composition of all three catalysts (Table S3). The results reveal that the N content is consistently low across all three catalysts, ranging from 1.2 to 1.5 at%, with no systematic variation with the Co:Zn ratio. Specifically, the N contents are 1.3 at% for Co:Zn=2:1,1.2 at% for Co:Zn=1:1, and 1.5 at% for Co:Zn=1:2, values that are essentially identical within experimental error. Critically, the N content shows no correlation with the observed product selectivity: the Co:Zn=2:1 catalyst (N=1.3 at%) yields CO with 80.4% FE, while the Co:Zn=1:2 catalyst (N=1.5 at%) yields HCOOH with 70.9% FE. This stark contrast definitively demonstrates that the trace residual nitrogen does not play a significant role in determining catalytic activity or product selectivity. The oxygen content, determined from the same XPS survey scans, ranges from 45.2 to 52.7 at%, reflecting the expected oxygen abundance in the metal oxide phases ($ZnCo_2O_4$ spinel and ZnO) and the silica support. The slight variation in O content correlates with the phase composition, the Zn-rich catalyst contains a higher proportion of ZnO and thus exhibits a slightly higher O content, which is entirely consistent with the intended oxide phase evolution. We therefore conclude that the observed selectivity switching is primarily governed by the Co:Zn ratio-dependent electronic structure modulation of the active metal sites, as evidenced by the systematic XPS binding energy shifts, rather than by trace residual nitrogen.

Table S3. Surface elemental compositions (at%) of the three CoZn oxide nanoflower catalysts determined by XPS survey scans.

Catalyst ID	Nominal Co:Zn ratio	C (at%)	O (at%)	Si (at%)	Co (at%)	Zn (at%)	N (at%)
1	≈ 1:1	26.5	48.5	14.2	4.5	5.1	1.2
2	≈ 2:1	28.3	45.2	15.6	6.8	2.8	1.3
3	≈ 1:2	23.8	52.7	12.3	2.2	7.5	1.5

Table S4 (new, Supporting Information): Rct values from equivalent circuit fitting for both electrolyte systems at each tested potential.

Potential (V)	Rct, $KHCO_3$ (Ω cm^2)	Rct, [EMIM]Cl-$KHCO_3$ (Ω cm^2)	Relative Difference (%)
-0.3	1250	680	45.6
-0.4	980	550	43.9
-0.5	720	420	41.7
-0.6	510	310	39.2
-0.7	380	240	36.8
-0.8	290	190	34.5
-0.9	220	150	31.8

The fitted (Rct value of 1250 $\Omega \cdot cm^2$ (pure $KHCO_3$, -0.3 V) is solved via nonlinear least-squares L-M iteration based on the full-spectrum EIS dataset:

The solution resistance Rs=15 $\Omega \cdot cm^2$ is fixed from high-frequency Nyquist intercept;
A residual function χ^2 is established to quantify the deviation between model-calculated impedance and experimental impedance across 10^{-1}-10^{-5};

The L-M algorithm iteratively optimizes Q_0, n, Rct and Warburg coefficient σ to minimize χ^2. The iteration converges at Rct =1250 $\Omega \cdot cm^2$;

For the [EMIM]Cl-$KHCO_3$ hybrid electrolyte at -0.3 V, identical fitting workflow yields a converged Rct =680 $\Omega \cdot cm^2$.

The large discrepancy between fitted Rct and the small visible arc in Figure 3a arises from the truncated horizontal axis range (0-50 $\Omega \cdot cm^2$), low-frequency Warburg diffusion tail that prevents semicircle closure, and the fact that fitting incorporates all full-frequency data rather than only the limited visible high-frequency fragment.

REFERENCE:

[1] Kresse, G.; Furthmüller, J. Efficiency of ab-initio total energy calculations for metals and semiconductors using a plane-wave basis set. *Computational Materials Science* **1996**, *6*, 15-50. https://doi.org/10.1016/0927-0256(96)00008-0.

[2] Blöchl, P. E.;Jepsen, O.; Andersen, O. K. Improved tetrahedron method for Brillouin-zone integrations. *Physical Review B* **1994**, *49*, 16223-16233. DOI: 10.1103/PhysRevB.49.16223.

[3] Perdew;Chevary;Vosko;Jackson;Pederson;Singh, M. S.; Fiolhais Atoms, molecules, solids, and surfaces: Applications of the generalized gradient approximation for exchange and correlation. *Physical review. B, Condensed matter* **1992**, *46 11*, 6671-6687.

[4] Grimme, S.;Antony, J.;Ehrlich, S.; Krieg, H. A consistent and accurate ab initio parametrization of density functional dispersion correction (DFT-D) for the 94 elements H-Pu. *The Journal of chemical physics* **2010**, *132 15*, 154104.

[5] Wang, V.;Xu, N.;Liu, J.-C.;Tang, G.; Geng, W.-T. VASPKIT: A user-friendly interface facilitating high-throughput computing and analysis using VASP code. *Computer Physics Communications* **2021**, *267*, 108033. DOI: https://doi.org/10.1016/j.cpc.2021.108033.

[6] Kühne, T. D.;Iannuzzi, M.;Del Ben, M.;Rybkin, V. V.;Seewald, P.;Stein, F.;Laino, T.;Khaliullin, R. Z.;Schütt, O.;Schiffmann, F.;Golze, D.;Wilhelm, J.;Chulkov, S.;Bani-Hashemian, M. H.;Weber, V.;Borštnik, U.;Taillefumier, M.;Jakobovits, A. S.;Lazzaro,

A.;Pabst, H.;Müller, T.;Schade, R.;Guidon, M.;Andermatt, S.;Holmberg, N.;Schenter, G. K.;Hehn, A.;Bussy, A.;Belleflamme, F.;Tabacchi, G.;Glöß, A.;Lass, M.;Bethune, I.;Mundy, C. J.;Plessl, C.;Watkins, M.;VandeVondele, J.;Krack, M.; Hutter, J. CP2K: An electronic structure and molecular dynamics software package - Quickstep: Efficient and accurate electronic structure calculations. *The Journal of Chemical Physics* **2020**, *152*. DOI: 10.1063/5.0007045 (acccessed 7/28/2026).

[7] Blöchl, P. E. Projector augmented-wave method. *Physical Review B* **1994**, *50*, 17953-17979. DOI: 10.1103/PhysRevB.50.17953.

[8] Perdew, J. P.;Burke, K.; Ernzerhof, M. Generalized Gradient Approximation Made Simple. *Physical Review Letters* **1996**, *77*, 3865-3868. DOI: 10.1103/PhysRevLett.77.3865.